ORIGINAL ARTICLE

Open Access

Performance analysis of frequency-mixed PPP-RTK using low-cost GNSS chipset with different antenna configurations

Xingxing Li[1,2], Hailong Gou[1], Xin Li[1,2*], Zhiheng Shen[1], Hongbo Lyu[3], Yuxuan Zhou[1], Hao Wang[1] and Qian Zhang[4]

Abstract

Low-cost Global Navigation Satellite System (GNSS) devices offer a cost-effective alternative to traditional GNSS systems, making GNSS technology accessible to a wider range of applications. Nevertheless, low-cost GNSS devices often face the challenges in effectively capturing and tracking satellite signals, which leads to losing the observations at certain frequencies. Moreover, the observation peculiarities of low-cost devices are in contradistinction to those of traditional geodetic GNSS receivers. In this contribution, a low-cost PPP-RTK model that considers the unique characteristics of different types of measurements is developed and its performance is fully evaluated with u-blox F9P receivers equipped with three distinctive antenna configurations: vertical dipole, microstrip patch, and helix antennas. Several static and kinematic experiments in different scenarios are conducted to verify the effectiveness of the proposed method. The results indicate that the mixed-frequency PPP-RTK model outperforms the traditional dual-frequency one with higher positioning accuracy and fixing percentage. Among the three low-cost antennas tested, the vertical dipole antenna demonstrates the best performance under static conditions and shows a comparable performance as geodetic antennas with a positioning accuracy of 0.02 m, 0.01 m and 0.07 m in the east, north, and up components, respectively. Under low-speed kinematic scenarios, the helix antenna outperforms the other two with a positioning accuracy of (0.07 m, 0.07 m, 0.34 m). Furthermore, the helix antenna is also proved to be the best choice for vehicle navigation with an ambiguity fixing rate of over 95% and a positioning accuracy of (0.13 m, 0.14 m, 0.36 m).

Keywords PPP-RTK, Low-cost device, Rapid ambiguity resolution, Centimeter-level positioning accuracy, Performance assessment

*Correspondence:
Xin Li
xinli@sgg.whu.edu.cn
[1] School of Geodesy and Geomatics, Wuhan University, 129 Luoyu Road, Wuhan 430079, Hubei, China
[2] Hubei Luojia Laboratory, Wuhan University, 129 Luoyu Road, Wuhan 430079, Hubei, China
[3] Tianjin Navigation Instrument Research Institute, 268 Dingzigu 1St Road, Tianjin 300130, China
[4] Meituan, 6 Wangjing East Road, Chaoyang District, Beijing, China

Introduction

Global Navigation Satellite System (GNSS) has been widely used in geodesy relying on geodetic receivers, which exhibit commendable capabilities in terms of multipath suppression, noise reduction, and observation quality. However, the widespread adoption of geodetic receivers is hindered by their high cost, bulky size, substantial power consumption, and inconvenient portability in the mass market. Thanks to the rapid advancements in manufacturing technology, GNSS receivers are undergoing a transformative shift towards miniaturization, lightweight design, and affordability (Amami et al.,

Li *et al. Satellite Navigation*   (2023) 4:26

Page 2 of 18

2014; Hofmann-Wellenhof et al., 2012). Many commercial companies such as Broadcom (www.broadcom.com), u-blox (www.u-blox.com), and unicorecomm (www.unicorecomm.com) have developed low-cost GNSS chipsets for as little as 100–200 dollars. This has made GNSS with low-cost receivers be a new research hotspot and of great potential for emerging massive and automatic applications (Mongrédien et al., 2016; Odolinski & Teunissen, 2016, 2017).

Numerous studies investigated the observation characteristics of low-cost receivers, including miniaturized GNSS boards like u-blox, entry-level NovAtel devices, and smartphones (Caldera et al., 2016; Chen & Qin, 2012; Li & Geng, 2019; Wanninger & Heßelbarth, 2020). The research indicated that the low-cost devices had higher noise level and lower carrier-to-noise-density ratio compared to the geodetic ones. Additionally, low-cost devices are characterized by severe systematic errors, such as the multipath (Gogoi et al., 2018; Zhang et al., 2019b), interfrequency bias (Håkansson et al., 2017), and inter-system bias (Mi et al., 2019). To better access these systematic errors, Zhang et al. (2021) developed an easily implementable method based on the ionosphere-corrected and geometry-free model, which is effective regardless the number of satellites and frequencies in most scenarios. Moreover, the quality of observations greatly relies on the receiving antenna. Cina and Piras (2015) reported that the combination of low-cost GNSS receivers with a geodetic antenna could improve their performance. Hamza et al. (2021) and Amami (2022) tested different types of antennas and illustrated their advantages and limitations. However, their studies focused mainly on the assessment of noise, and more detailed analysis is required.

As to positioning capability, several studies were conducted to evaluate the performance of low-cost GNSS receivers. Takasu and Yasuda (2008, 2009) were the pioneers in evaluating the Real-Time Kinematic (RTK) performance and demonstrated that RTK method using the low-cost GNSS receivers could achieve comparable performances with geodetic grade receivers under favorable circumstances. The similar conclusions were drawn by Jo et al. (2013), Cina and Piras (2015), and Garrido-Carretero et al. (2019). Unlike the RTK algorithm, Precise Point Positioning (PPP) technology can achieve centimeter-level positioning accuracy using only a single GNSS receiver. Gill et al. (2017) assessed the single-frequency PPP performance with the ionospheric products provided by the Centre National d'Etudes Spatiales (CNES). Following this, the ionosphere-weighted PPP model (Li et al., 2019) to identify various situations with the different uncertainties

of ionospheric constraints was addressed. Wen et al. (2020) and Wang et al. (2021) utilized the observations from smart devices to conduct PPP. Furthermore, Li and Geng (2022) enhanced the ambiguity resolution method for Android data. Considering the coexistence of single- and dual-frequency observations on low-cost GNSS devices, Nie et al. (2020) employed the single-frequency ionosphere-corrected code measurements and the conventional dual-frequency ionosphere-free code and phase measurements, shorterning PPP convergence time to a few minutes.

Both RTK and PPP technologies using low-cost devices have their own pros and cons. To achieve rapid and accurate positioning for a wide range of users, researchers proposed a combined approach called PPP-RTK (Li et al., 2011; Teunissen et al., 2010; Wübbena et al., 2005). The PPP-RTK technique has the merits of flexibility, high accuracy, extensive coverage, and enhanced privacy protection, making it as a promising tool with innovative opportunities for emerging mass applications. Notably, scholars have explored PPP-RTK using low-cost devices. Nadarajah et al. (2018) investigated the PPP-RTK performance with low-cost single-frequency U-blox M8 receivers and found that 5cm accuracy could be achieved within 9 min using the data with a 30-s sampling interval. Li et al. (2022) demonstrated the feasibility of PPP-RTK using android GNSS raw measurements with an external antenna, revealing the potential for instantaneous decimeter-level positioning accuracy under low-speed dynamic conditions. However, there are still some challenges in PPP-RTK with low-cost devices. Firstly, data loss often occurs due to the hardware constraints of low-cost devices. Effectively utilizing all available data becomes crucial. Secondly, the disparities in observation characteristics between low-cost and high-end devices render the traditional stochastic model inadequate, necessitating the determination of appropriate weight ratios. Additionally, there are various types of low-cost antennas in market, such as helix antennas, microstrip patch antennas, and vertical dipole antennas, which have different performances depending on the manufacturing process and physical structure (Amami et al., 2014; Bancroft, 2019). Therefore, further exploration of low-cost devices' PPP-RTK performance is urgently needed.

In this contribution, we implement PPP-RTK with low-cost devices and evaluate their performance. A mixed-frequency PPP-RTK model and a modified stochastic model considering the prior knowledge of different types of measurements are proposed. In addition, the signal characteristics and positioning performance of different low-cost devices are compared and analyzed. After this

Li *et al. Satellite Navigation*   (2023) 4:26

Page 3 of 18

introduction, the PPP-RTK system with low-cost devices is first described. Then the experimental sets and the processing strategies are detailed. Hereafter, the effectiveness of the method proposed in this study and the performance of different low-cost devices are evaluated. Finally, conclusions are summarized.

Methodology

In this section, the implementation of the mixed-frequency PPP-RTK model and the cascade ambiguity resolution strategy are introduced first. A stochastic model considering the prior information on low-cost GNSS devices is then detailed.

Mixed-frequency PPP-RTK model

The performances of low-cost GNSS devices are compromised in some functions, such as preamplifier, Digital Signal Processing (DSP), and Low Noise Amplifier (LNA), resulting in the loss of observations, particularly on the second band in certain periods. To address this limitation, this paper proposes a mixed-frequency PPP-RTK model that leverages all available observation information to improve positioning performance. As illustrated in Fig. 1, the model comprises two main components: the server and the client. The former provides the precise atmospheric corrections derived from ambiguity-fixed PPP solutions with the precise orbit, clock, and Uncalibrated

$$
\begin{aligned}
P_{\mathrm{r},i}^{\mathrm{s}} &= \rho_{\mathrm{r}}^{\mathrm{s}} + c \cdot \left(t_{\mathrm{r}} - t^{\mathrm{s}}\right) + \gamma_i^{\mathrm{s}} \cdot I_{\mathrm{r},1}^{\mathrm{s}} + m_{\mathrm{r}}^{\mathrm{s}} \cdot Z_{\mathrm{r}} \\
&\quad + \left(b_{\mathrm{r},i} - b_i^{\mathrm{s}}\right) + e_{\mathrm{r},i}^{\mathrm{s}} \\
L_{\mathrm{r},i}^{\mathrm{s}} &= \rho_{\mathrm{r}}^{\mathrm{s}} + c \cdot \left(t_{\mathrm{r}} - t^{\mathrm{s}}\right) + \lambda_i \cdot N_{\mathrm{r},i}^{\mathrm{s}} - \gamma_i^{\mathrm{s}} \cdot I_{\mathrm{r},1}^{\mathrm{s}} \\
&\quad + m_{\mathrm{r}}^{\mathrm{s}} \cdot Z_{\mathrm{r}} + \left(B_{\mathrm{r},i} - B_i^{\mathrm{s}}\right) + \varepsilon_{\mathrm{r},i}^{\mathrm{s}}
\end{aligned}
\tag{1}
$$

where $\rho_{\mathrm{r},i}^{\mathrm{s}}$ is the geometric distance between the receiver r and the satellite s; t_{r} and t^{s} denote clock offset at the receiver and satellite side respectively in seconds scaled by the light speed in vacuum c; $I_{\mathrm{r},1}^{\mathrm{s}}$ refers to the slant ionospheric delay at the first frequency linked to other frequencies by $\gamma_i = \lambda_i^2/\lambda_1^2$ with the wavelength λ_i; the zenith tropospheric delay Z_{r} is mapped to the slant direction by the function $m_{\mathrm{r}}^{\mathrm{s}}$; the integer ambiguity $N_{\mathrm{r},i}^{\mathrm{s}}$ is in cycles scaled by the wavelength λ_i; $b_{\mathrm{r},i}$ and $B_{\mathrm{r},i}$ denote the receiver hardware biases in pseudorange and carrier phase observations, respectively, while b_i^{s} and B_i^{s} are satellite counterparts; $e_{\mathrm{r},i}^{\mathrm{s}}$ and $\varepsilon_{\mathrm{r},i}^{\mathrm{s}}$ represent measurement noise of pseudorange and carrier phase, respectively. Other errors such as the satellite and receiver antenna Phase Center Offsets (PCOs) and Phase Center Variations (PCVs), the relativistic effects, the tidal loadings, and the phase wind-up effect are corrected by the existing models (Kouba, 2009).

Considering the coexistence of single-, dual-, multifrequency GNSS observations using low-cost devices, the uncombined PPP-RTK model with the atmospheric constraints can be expressed as:

$$
\begin{cases}
\begin{pmatrix} \mathrm{E}\!\left(\boldsymbol{p}_{\mathrm{r}}^{\mathrm{s,sys}}\right) \\ E\!\left(\boldsymbol{l}_{\mathrm{r}}^{\mathrm{s,sys}}\right) \end{pmatrix} = \begin{pmatrix} \boldsymbol{L}_{\mathrm{u}} & c \cdot \boldsymbol{I}_{\mathrm{V}} & \boldsymbol{I} & \boldsymbol{O} & \boldsymbol{\gamma}^{\mathrm{s,sys}} & m_{\mathrm{r,w}}^{\mathrm{s,sys}} \cdot \boldsymbol{I}_{\mathrm{V}} & \boldsymbol{I}_{\mathrm{V}} \\ \boldsymbol{L}_{\mathrm{u}} & c \cdot \boldsymbol{I}_{\mathrm{V}} & \boldsymbol{I} & \boldsymbol{\lambda} & -\boldsymbol{\gamma}^{\mathrm{s,sys}} & m_{\mathrm{r,w}}^{\mathrm{s,sys}} \cdot \boldsymbol{I}_{\mathrm{V}} & \boldsymbol{O} \end{pmatrix} \begin{pmatrix} \boldsymbol{X}_{\mathrm{u}} \\ \bar{t}_{\mathrm{r}}^{\mathrm{G}} \\ \boldsymbol{b}_F \\ \overline{\boldsymbol{N}}_{\mathrm{r}}^{\mathrm{s}} \\ \delta I_{r,1}^{\mathrm{s}} \\ \delta Z_{\mathrm{r,w}} \\ S_{\mathrm{r}}^{\mathrm{sys\text{-}G}} \end{pmatrix} \\[4ex]
\boldsymbol{H} = \begin{pmatrix} H_1 & H_2 & \dots & H_k \end{pmatrix}^{\mathrm{T}}, \ \boldsymbol{H} = \boldsymbol{p}_{\mathrm{r}}^{\mathrm{s}}, \boldsymbol{l}_{\mathrm{r}}^{\mathrm{s}}, \boldsymbol{b}_F, \overline{\boldsymbol{N}}_{\mathrm{r}}^{\mathrm{s}}, \dots
\end{cases}
\tag{2}
$$

Phase Delays (UPD) products (Li et al., 2021; Psychas & Verhagen, 2020). The latter establishes an uncombined observation model (Geng et al., 2020; Zhang et al., 2019a) that incorporates single-, dual-, and multi-frequency observations. The rapid ambiguity resolution in the mixed-frequency mode is then performed with the assistance of the atmospheric corrections provided by the server component.

For a receiver r which tracks a satellite s of system sys at frequency i, the GNSS pseudorange measurement $(P_{\mathrm{r},i}^{\mathrm{s}})$ and carrier phase measurement $(L_{\mathrm{r},i}^{\mathrm{s}})$ can be described as:

$$
\begin{cases}
p_{\mathrm{r},i}^{\mathrm{s}} = f_{\mathrm{omc}}\!\left(P_{\mathrm{r},i}^{\mathrm{s}} - f_{\mathrm{aug}}\!\left(P_{\mathrm{r},i}^{\mathrm{s}}\right)\right) \\[1ex]
l_{\mathrm{r},i}^{\mathrm{s}} = f_{\mathrm{omc}}\!\left(L_{\mathrm{r},i}^{\mathrm{s}} - f_{\mathrm{aug}}\!\left(L_{\mathrm{r},i}^{\mathrm{s}}\right)\right) \\[1ex]
\bar{t}_{\mathrm{r}}^{\mathrm{G}} = t_{\mathrm{r}}^{\mathrm{G}} + b_{\mathrm{r,IF12}} \\[1ex]
\overline{N}_{\mathrm{r},i}^{\mathrm{s}} = N_{\mathrm{r},i}^{\mathrm{s}} + d_{\mathrm{r},i} \\[1ex]
f_{\mathrm{aug}}\!\left(P_{\mathrm{r},i}^{\mathrm{s}}\right) = m_{\mathrm{r,w}}^{\mathrm{s}} \cdot Z_{\mathrm{r,w}} + \gamma_i \cdot \bar{I}_{\mathrm{r},1}^{\mathrm{s}} \\[1ex]
f_{\mathrm{aug}}\!\left(L_{\mathrm{r},i}^{\mathrm{s}}\right) = m_{\mathrm{r,w}}^{\mathrm{s}} \cdot Z_{\mathrm{r,w}} - \gamma_i \cdot \bar{I}_{\mathrm{r},1}^{\mathrm{s}}
\end{cases}
\tag{3}
$$
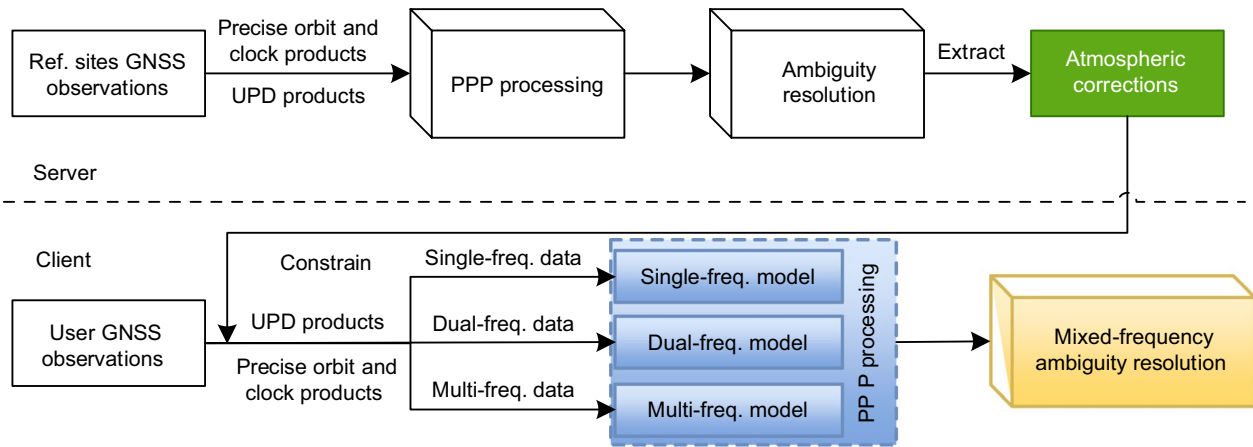
Fig. 1 Workflow of mixed-frequency PPP-RTK model

$$
\begin{cases}
\bar{I}^{s}_{r,1} = I^{s}_{r,1} - \beta_{12} \cdot \left(b_{r,1} - b_{r,2}\right) \\[2mm]
b_{r,\mathrm{IF12}} = \alpha_{12} \cdot b_{r,1} + \beta_{12} \cdot b_{r,2} \\[2mm]
d_{r,i} = B_{r,i} - \dfrac{\left(b_{r,\mathrm{IF12}} - \gamma^{s}_{i} \cdot \beta_{12} \cdot (b_{r,1} - b_{r,2})\right)}{\lambda_{i}} \\[3mm]
\alpha_{12} = \dfrac{f_1^2}{f_1^2 - f_2^2} \\[3mm]
\beta_{12} = -\dfrac{f_2^2}{f_1^2 - f_2^2}
\end{cases}
\tag{4}
$$

where $\mathrm{E}(\cdot)$ denotes the expectation operator; $p^{s}_{r,i}$ and $l^{s}_{r,i}$ represent the observed-minus-computed code and phase observations after the removal of the atmospheric corrections $f_{\mathrm{aug}}\left(P^{s}_{r,i}\right)$ and $f_{\mathrm{aug}}\left(L^{s}_{r,i}\right)$, respectively; H (the representative of $p^{s}_{r}, l^{s}_{r}, \overline{N}^{s}_{r}, \ldots$) is a column vector whose number of rows depends on the number of frequencies k; X_{u} and L_{u} represent the user coordinates to be estimated and the design matrix after linearization, respectively; I_{V} is a column vector with all elements of 1; I and O are identity matrix and zero matrix, respectively. The satellite clock offsets t^{s} have been corrected with the International GNSS Service (IGS) precise products. $\bar{t}^{G}_{r}$ denotes the receiver clock offset absorbing the liner combination of receiver hardware biases $b_{r,\mathrm{IF12}}$. $\overline{N}^{s}_{r}$ refers to the vector of the float ambiguities $(\overline{N}^{s}_{r,i})$, which can recover its integer feature by deducting the hardware delay $d_{r,i}$ with the assistance of UPD products. Since the tropospheric hydrostatic delay can be corrected by the existing models, only the wet component $Z_{r,w}$ remains unknown. $f_{\mathrm{aug}}\left(P^{s}_{r,i}\right)$ and $f_{\mathrm{aug}}\left(L^{s}_{r,i}\right)$ represent the precise atmospheric corrections, which contain the tropospheric wet delay $(Z_{r,w})$ and ionospheric delay with hardware delay at the receiver side $(\bar{I}^{s}_{r,1})$. $\delta I^{s}_{r,1}$ and $\delta Z_{r,w}$

denote the residual of the slant ionospheric delay on the first frequency and the tropospheric zenith wet delay, respectively. The numbers 1, 2 represent the two frequencies used in the satellite clock offset estimation process. However, if the frequency of the observation does not correspond to these frequencies, the inter-frequency bias b_{F} must be considered. Moreover, the receiver inter-system bias $S^{\mathrm{sys}\text{-}\mathrm{G}}_{r}$ is introduced for each system except for Global Positioning System (GPS) under the assumption that the multi-GNSS code observations share the same receiver clock. Thus, the parameters X to be estimated can be written as follows:

$$
X = \left(X_{u}, \bar{t}^{G}_{r}, b_{F}, S^{\mathrm{sys}\text{-}\mathrm{G}}_{r}, \delta I^{s}_{r,1}, \delta Z_{r,w}, \overline{N}^{s}_{r}\right)^{\mathrm{T}}
\tag{5}
$$

where $X_{u}, \bar{t}^{G}_{r}$ are estimated as a white noise model, and $b_{F}, S^{\mathrm{sys}\text{-}\mathrm{G}}_{r}, \overline{N}^{s}_{r}$ are estimated as a random walk model. By correcting atmospheric products, the prior knowledge of $\delta I^{s}_{r,1}$ and $\delta Z_{r,w}$ are set to zero with high precision, which can be expressed as:

$$
\begin{cases}
\delta I^{s}_{r,1} = 0, & \sigma^{2}_{\delta I^{s}_{r,1}} \\[2mm]
\delta Z_{r,w} = 0, & \sigma^{2}_{\delta Z_{r,w}}
\end{cases}
\tag{6}
$$

Note that the ionospheric corrections absorb the hardware delays, which brings additional biases to the user side and needs to be carefully considered. The satellite-induced bias remains consistent in both the server and user ends, thereby will not affect the positioning. However, the receiver-induced bias varies with stations. Once only single-frequency observations are used, this bias could be absorbed by the estimated receiver clock and ambiguity parameters. While for dual-frequency or mixed-frequency processing, an additional

Li *et al. Satellite Navigation*   (2023) 4:26

Page 5 of 18
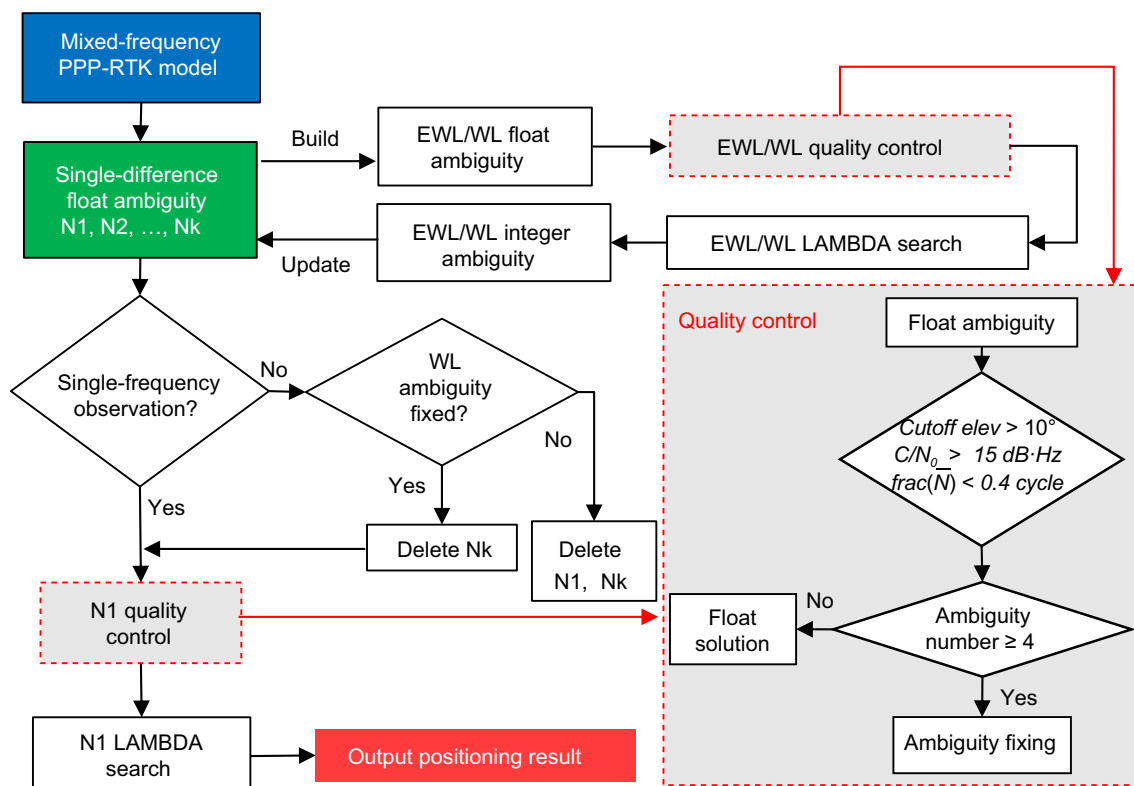
Fig. 2 Workflow of mixed-frequency ambiguity resolution

frequency-dependent code bias should be estimated for PPP-RTK users.

With the assistance of precise atmospheric corrections, a rapid ambiguity resolution can be achieved. For the combined use of single-, dual-, and multi-frequency ambiguities, a cascade mixed-frequency ambiguity resolution strategy is conducted in Fig. 2. The float ambiguities derived from the above PPP-RTK model will be divided into three categories: the multi-frequency one, the dual-frequency one, and the single-frequency one. When there are more than two ambiguities, the Extra-Wide-Lane (EWL) and Wide-Lane (WL) ambiguities are formulated and fixed using the Least-Square AMBiguity Decorrelation Adjustment (LAMBDA) method (Temiissen, 1995) in sequence. When there are two ambiguities, only WL ambiguities are considered. The integer EWL ambiguities will be taken as virtual observations in the parameter estimation for accelerating the search process of WL ambiguities, and integer WL ambiguities will also serve as virtual observations for N1 ambiguity determination. Then N1 ambiguity resolution will be conducted also using the LAMBDA method. Note that multi- and dual-frequency ambiguities that are not fixed in WL mode will be removed in the next step. For the single-frequency ambiguities, they are fixed directly

after correcting the UPD. To improve the success rate of ambiguity resolution, some quality control measures are employed to select the proper candidates for fixing, wherein the cutoff elevation, the minimum carrier-to-noise-density ratio C/N_0, and the maximum fractional part of ambiguity are set as the threshold. If the number of ambiguities after N1 ambiguity quality control is less than four or LAMBDA search fails, float solutions will be output.

Modified stochastic model considering the prior measurement accuracy

As the functional model describes the relationship between GNSS raw measurements and the parameters to be estimated, the observation stochastic model depicts the expectation and probability distribution of the random errors of measurements by defining a variance matrix, which is of great importance for parameter estimation and integer ambiguity resolution (Teunissen, 2018; Wang et al., 2002).

When low-cost GNSS devices are used for positioning in complex urban scenes, the traditional stochastic model using the elevation weighting scheme is no longer applicable as the satellites with high elevation may even

Li *et al. Satellite Navigation*   (2023) 4:26

Page 6 of 18

be blocked. In contrast, the carrier-to-noise-density ratio (C/N_0), which is closely associated with the propagation path of the signal, is a better choice for defining the variance matrix. Moreover, the GNSS signal strength depends greatly on the type of receiver and antenna, which may vary significantly when equipped with different low-cost devices. In this way, to better account for the actual situation in defining the variance matrix, a modified stochastic model is given below:

$$\sigma_i = \sqrt{C_0 \times 10^{-\frac{C/N_0}{C_1}}} \qquad (7)$$

where C_0 and C_1 are the fitting parameters determined based on the prior observation information, and σ is the measurement precision determined by C/N_0 with the unit in dB·Hz.

In order to obtain the appropriate fitting parameters C_0 and C_1, the long-term observations of different types of GNSS devices are collected and tested in advance. The zero-baseline (or ultra-short baseline) method is applied to evaluate the noise of pseudorange observation in the condition that the satellite orbit error and clock offset error are eliminated, and the effect of atmospheric delay is alleviated (Amiri-simkooei & Tiberius, 2007; Pirazzi et al., 2017). The formula to evaluate the noise level of code observations is shown as follows:

$$\Delta e^s_{r_1 r_2, f} = \Delta P^s_{r_1 r_2, f} - \sum_{i=1}^{n} \Delta P^{s_i}_{r_1 r_2, f}/n \qquad (8)$$

where r_1 is the reference station, and Δ denotes the single-difference operator. The receiver clock offset is equal to the mean value of all satellites' code single-difference residual $(\Delta P^s_{r_1 r_2, f})$ at the current epoch. After subtracting the receiver clock offset from the code single-difference residual, the code noise $\Delta e^s_{r_1 r_2, f}$ is acquired.

After the computation of the measurement noise, the relationship between the noise and C/N_0 is addressed. We divide the C/N_0 into sections with an interval of 1 dB·Hz and calculate the mean value of the code noise at a specific section. As shown in Eq. (9), the least squares method is used to estimate the fitting parameters C_0, C_1.

Table 1 The fitting result of helix antenna

Fitting result	GPS parameters	Galileo parameters	BDS parameters
C_0	153.932	45.806	2333.439
C_1	12.431	16.434	8.805

where $\tilde{\sigma}$ refers to the residual of code observation noise, which equals the real code observation noise (σ) minus the first term of Taylor expansion (σ^0). L_0 and L_1 represent the coefficient of the parameters C_0 and C_1 respectively after linearization. C_0^0 and C_1^0 are the approximate values of the parameters to be estimated $(C_0$ and $C_1)$, respectively.

The fitting curves and results of helix antenna are taken as examples and shown in Fig. 3 and Table 1. Galileo and BDS of Fig. 3 represent Galileo navigation satellite system and BeiDou Navigation Satellite System, respectively. In this study, the weight of code observations was determined first, followed by the weight of phase observations, which was determined based on the empirical ratio of 100:1 of phase measurement accuracy to code measurement accuracy.

Data collection and experiment design

In this section, several experiments were designed for the verification and performance evaluation of the proposed PPP-RTK model using low-cost GNSS devices. The detailed information on GNSS devices including GNSS boards and antennas is shown in Table 2. A geodetic GNSS board (Septentrio PolarRx5S) and a geodetic-grade antenna (Trimble Zephyr 2), named SEPT + Trimble, was employed as a benchmark. Three types of low-cost GNSS devices: u-blox ZED-F9P GNSS board together with Vertical Dipole Antenna (VDA), Microstrip Patch Antenna (MPA), and Helix Antenna (HA) named as F9P + VDA, F9P + MPA, and F9P + HA, respectively were tested and compared. In kinematic experiments, a terminal that consists of a low-cost GNSS board (u-blox ZED-F9P) together with

$$\begin{cases} E(\tilde{\sigma}) = L_0 \times C_0 + L_1 \times C_1 \\ \tilde{\sigma} = \sigma - \sigma^0 \\ L_0 = 10^{-\frac{C/N_0}{C_1^0}}/2 \times \sqrt{C_0^0 \times 10^{-\frac{C/N_0}{C_1^0}}} \\ L_1 = \ln 10 \times 10^{-\frac{C/N_0}{C_1^0}} \times C_0^0 \times C/N_0 \times C_1^{0-2}/2 \times \sqrt{C_0^0 \times 10^{-\frac{C/N_0}{C_1^0}}} \end{cases} \qquad (9)$$

Li *et al. Satellite Navigation*　　(2023) 4:26

Page 7 of 18
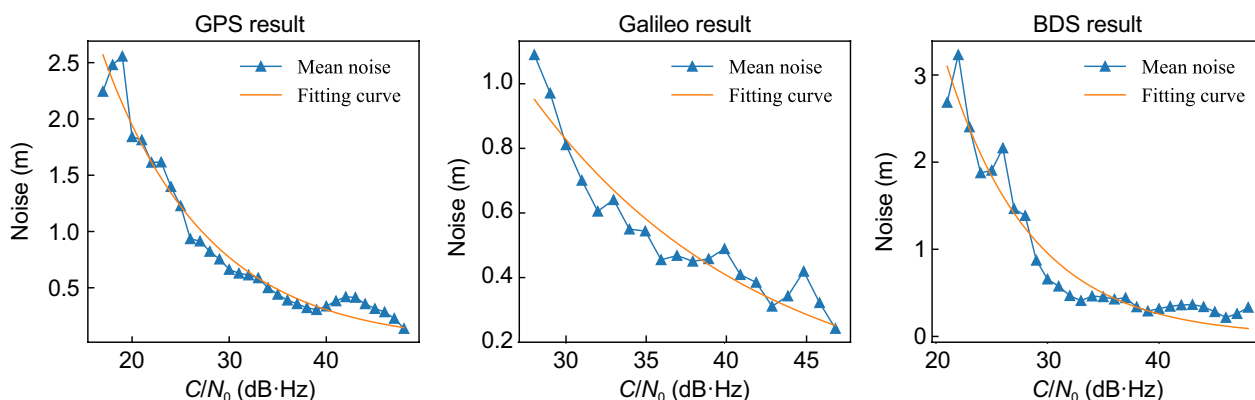
Fig. 3 Fitting curves of helix antenna. The blue triangle and the orange line denote the raw mean value of noise and the fitting curve, respectively

a geodetic-grade antenna (Trimble Zephyr 2), named F9P + Trimble was added as supplementary verification. The low-cost GNSS devices all support GPS (L1 and L2), Galileo (E1 and E5b), and BDS (B1I and B2I) signals with a sampling interval of 1 s. Among the four types of GNSS antennas, the signal gain of MPA and HA (28–35 dB) antennas is much lower than that of Trimble (50 dB), but they are much cheaper ($25–$50) and more affordable in the mass market.

To evaluate the positioning performance, experiments were conducted in both static and kinematic modes. The static experiment was carried out from GPS Time (GPST) 12:00 to 22:00 on Day of Year (DOY) 334 (November 30th), 2021, with the experimental devices placed on the roof of a building, as shown in subgraph a of Fig. 4. The surrounding environment, including trees and tall buildings, as shown in subgraph b of Fig. 4, could potentially disrupt GNSS signals.

In addition to the static experiment, two kinematic tests were conducted to validate the low-cost PPP-RTK method. Experiment A took place on the playground from GPST 8:35 to 9:00 on DOY 017 (January 17th), 2022. Experiment B is a vehicle experiment conducted in a semi-urban environment from GPST 6:50 to 7:20 on DOY 12 (January 12th), 2022. The subgraphs a, b and c in Fig. 5 depict the experimental equipment and the trajectory of the two tests, respectively. For the kinematic experiments, the tightly coupled multi-GNSS RTK/INS solutions calculated by commercial Inertial Explorer (IE) 8.9 software (NovAtel, 2018) using the raw observation of the tactical-level IMU and GNSS terminals were taken as the reference coordinates.

Table 3 provides a detailed processing strategy for the PPP-RTK scheme. The multi-GNSS observations (GPS, Galileo, and BDS) with a sampling interval of 1 s were employed. In addition, the precise products from the German Research Centre for Geosciences (GFZ) were used to correct the orbit and clock offset errors, while the satellite phase biases were computed from a set of globally distributed stations using open-source software called GREAT-UPD (Li et al., 2021). Figure 6 shows the reference station network, which generates the atmospheric corrections for the clients.

Results and discussion

In this section, we first evaluate the observation quality of different low-cost devices in terms of data availability, C/N_0, noise level, and cycle slip. Then the performances of PPP-RTK with different low-cost devices in static and kinematic conditions are investigated.

Observation characteristics of different low-cost GNSS devices

To figure out the observation characteristics of various low-cost GNSS devices, the data availability, C/N_0, observation noise, and cycle slip rate with different low-cost devices are analyzed successively.

Firstly, the availability of observations is analyzed to explore the sensitivity and stability of the different low-cost GNSS devices. Figure 7 shows the availability of the code and phase observations on the second band of GNSS (e.g., GPS L2, BDS B2I, Galileo E5a), represented by the red and blue lines, respectively. Noting that the Septentrio GNSS receiver can track BDS Geosynchronous Earth Orbit (GEO) satellites from C01 to C05, while they are unavailable for the u-blox F9P due to the differences in inner acquisition algorithms and thresholds. For low-cost antennas, the observation continuity and integrity of some satellites, such as G26, E04 and E24, are inferior compared to the Trimble antenna. Overall, the analysis suggests that the performance in tracking satellites is largely determined by the GNSS boards used, while the continuity and integrity

Li *et al. Satellite Navigation*　　(2023) 4:26

Page 8 of 18

Table 2 The information of GNSS devices used in this study

Mark name	GNSS board	Antenna	Antenna characteristics
SEPT + Trimble	Septentrio PolaRx5S (SEPT)	Trimble Zephyr 2	Geodetic antenna: $D = 152$ mm; $H = 74$ mm Signal gain: 50 dB Weight: 590 g Price: \$2500–\$3000 (2022)
F9P + Trimble	u-blox ZED-F9P (F9P)	HG-GOYH7151 (VDA)	
F9P + VDA			Vertical dipole antenna: $D = 150$ mm; $H = 63.7$ mm Signal gain: (40 ± 2) dB Weight: 425 g Price: \$50–\$100 (2022)
F9P + MPA		HG-GOYH3062 (MPA)	Microstrip patch antenna: $D = 80$ mm; $H = 21.2$ mm Signal gain: (30 ± 2) dB Weight: ≤ 150 g Price: \$25–\$50 (2022)
F9P + HA		HX-CH7604A (HA)	Helix antenna: $D = 27.5$ mm; $H = 59$ mm Signal gain: (33 ± 2) dB Weight: ≤ 25 g Price: \$25–\$50 (2022)

Note that the letters "*D*" and "*H*" represent the diameter and height of the antenna, respectively. The "±" sign indicates a range of values. For example, (40 ± 2) dB indicates a maximum signal gain of 42 dB and a minimum signal gain of 38 dB

of observations much depend on the type of antenna employed.

Table 4 reveals the percentage of single-frequency data in different scenarios. Notably, in the case of the campus playground, which is surrounded by dense trees and buildings, the single-frequency data accounts for the largest proportion. Conversely, in the vehicle experiment, where the car traversed a road section with a wide field of vision for nearly 20 min, the proportion of single-frequency data is comparatively smaller. Among the tested GNSS terminals, SEPT + Trimble exhibits the smallest proportion of single-frequency data, followed by F9P + Trimble, while the remaining low-cost terminals show similar proportions of single-frequency data. This indicates that low-cost boards and the environment significantly influence data tracking capabilities.

Figure 8 illustrates the C/N_0 values on the first band of GPS (L1) for four types of GNSS terminals: SEPT + Trimble, F9P + VDA, F9P + MPA, and F9P + HA, represented by red, blue, green, and orange, respectively. A box diagram is drawn to demonstrate the distribution of the C/N_0 for every 15° interval. The C/N_0 values are rising with the increase of the elevation angles. When the elevation is larger than 45°, the C/N_0 values of the four types of GNSS terminals exceed 40 dB·Hz. Owing to the high gain of the Trimble antenna, the SEPT + Trimble shows the best performance in signal intensity (Amami, 2022; Huang, 2022). It is worth noting that the C/N_0 of HA is higher than that of the other two low-cost antennas and is even comparable to that of Trimble when the elevation is below 45°. It suggests that the HA's high C/N_0 value may be attributed to its stronger tracking characteristics for low-elevation satellites.
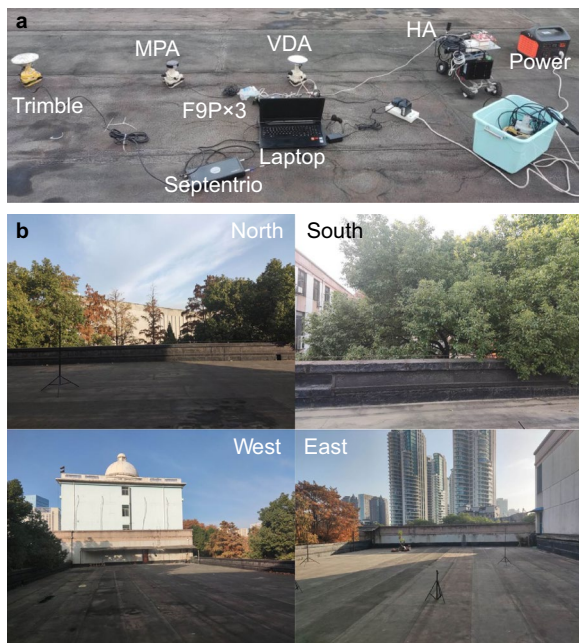
Fig. 4 Experimental devices and surrounding environment in the static experiment. **a** depicts the experimental devices; **b** represents the surrounding environment in the static experiment

Figure 9 demonstrates the code and phase noises of four GNSS terminals on the first band of GPS (L1), where the code noise is evaluated by the multipath combination (Kleusberg & Teunissen, 1996), and phase noise is calculated by the cubic difference between epochs (Amiri-Simkooei & Tiberius, 2007). The SEPT + Trimble device demonstrates superior performance, exhibiting smaller code and phase noise Root Mean Square (RMS) values of 0.302 and 0.005 m, respectively, compared to the three

low-cost GNSS devices. For the low-cost GNSS devices, the RMS values for code noise of F9P + VDA, F9P + MPA, and F9P + HA are 0.3, 1.6, and 1.0 m, respectively, while RMSs for the phase noise of all three antennas are comparable, about 0.007 m. Note that the systematic and periodic deviations are observed in the code observations of F9P + MPA and F9P + HA, which lead to higher RMS values. One can conclude that under static conditions microstrip patch antenna is most vulnerable to noise and multipath interference, while vertical dipole antenna is of the best multipath suppression ability among the three low-cost GNSS antennas.

Figure 10 displays the code and phase observation noise series of different GNSS devices in real-world kinematic scenarios. In such situations, GNSS signals are particularly susceptible to interference or interruption, leading to multiple outliers in GNSS observations. This problem will be more pronounced when low-cost antennas are employed (Kaplan & Hegarty, 2017). As a result, the RMS of code noise for SEPT + Trimble and F9P + Trimble is 1.6 m, while it rises to 2.7 m, 2.8 m, and 1.8 m for F9P + VDA, F9P + MPA, and F9P + HA, respectively. In general, the noise level of phase measurement for the four terminals is comparable.

Moreover, the cycle slip rate, which is calculated as the percentage of the epochs with cycle slip over the total epochs, is also a key indicator for assessing carrier phase measurement. Table 5 shows the number of cycle slips and cycle slip rates of different GNSS devices under the static and the kinematic scenarios. As expected, cycle slips are more likely to occur on low-cost GNSS boards under kinematic conditions. For instance, the u-blox F9P receiver with a Trimble or a helix antenna exhibits a cycle slip rate of around 25‰ in the kinematic scenario, which is 3.6 times larger than that of SEPT + Trimble. Notably,
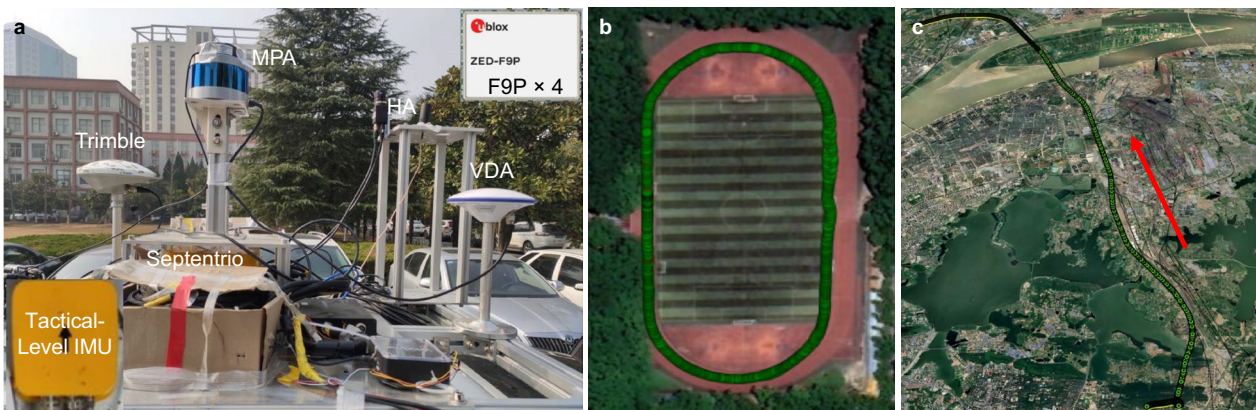
Fig. 5 Equipment and trajectory of the two experiments. **a** depicts the experimental devices in the kinematic experiments; **b** and **c** represent the trajectory of Experiment A and Experiment B, respectively

Li *et al. Satellite Navigation*   (2023) 4:26

Page 10 of 18

Table 3 Processing strategies for PPP-RTK

Item	Model
GNSS system	GPS, Galileo, and BDS
Signal section	GPS: L1/L2; Galileo: E1/E5b; BDS: B1I/B2I
Sampling rate	1 s
Elevation cut-off angle	7°
Weight for observations	The modified stochastic model proposed in this paper
Phase wind-up effect	Corrected
Ionospheric delay	Corrected by atmospheric corrections
Tropospheric delay	The dry component was corrected by the Saastamoinen model; the wet component was corrected by atmospheric corrections
Satellite and receiver antenna phase center	igs14.atx
Station coordinate	Estimated in the epoch-wise kinematic model
Phase ambiguity	Partial ambiguity resolution strategy proposed in this paper
Atmospheric corrections	Generated by the server stations, the distance between the server stations and user stations is about 50–60 km
Real-time or offline	Real-time
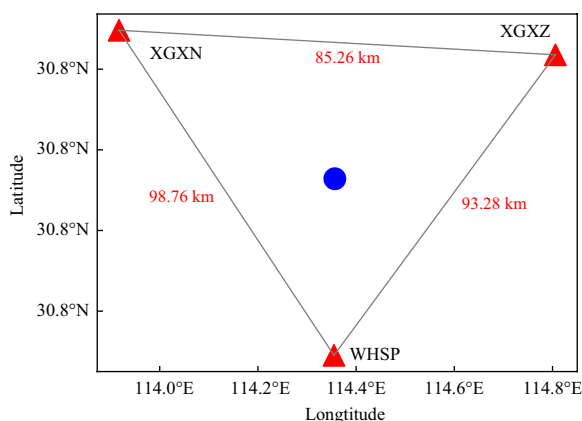
Fig. 6 The reference station network. The red triangles and blue dots represent the reference and user stations, respectively

among the three low-cost antennas, the helix antenna demonstrates the best performance.

Additionally, Table 6 demonstrates the performance ranking of different low-cost devices in terms of C/N_0, noise level, and cycle slip rate. The results show that the helix antenna exhibits the best performance in terms of C/N_0 and cycle slip rate. As for the noise level, the vertical dipole antenna and the microstrip patch antenna perform slightly better under static and kinematic conditions, respectively.

PPP-RTK performance in static experiments

Figure 11 illustrates the positioning error series and satellite numbers (NSAT) using a low-cost u-blox receiver with a microstrip patch antenna. It is evident that our

PPP-RTK method achieves rapid and consistent centimeter-level positioning accuracy for most of the 7-h period. In contrast, traditional dual-frequency PPP-RTK is prone to the occlusions from the surrounding environment, leading to several reductions in the number of available satellites and reconvergence processes as depicted in Fig. 4. The performance degradation is alleviated using our proposed mixed-frequency PPP-RTK system, which demonstrates superior accuracy and stability. Table 7 further presents the fixed rate and positioning accuracy. The 3D-RMS with our new method is reduced from 0.53 m of the traditional method to 0.07 m, an improvement by 86.8%. In the traditional dual-frequency model, if only the single-frequency signal of a satellite is received, the satellite will be abandoned. Limited by the hardware performance of low-cost equipment, there are few observations available in some epochs with the traditional dual-frequency model. By contrast, the proposed mixed-frequency method can fully use all available measurements, and thus outperforms the traditional approach.

Compared with a survey-grade device, the positioning series with the new PPP-RTK method for three types of low-cost GNSS terminals (F9P + VDA, F9P + MPA, F9P + HA) is further presented in Fig. 12. The number of available satellites (NSAT), position dilution of precision (PDOP), and fixing status of each epoch is also given in this figure. It is worth noting that the low-cost GNSS devices can achieve the similar positioning accuracy as the geodetic one when the number of satellites is more than ten. However, the positioning performance significantly degrades when the number of the satellites decreases to about five, as illustrated in the second red box of Fig. 12. Moreover,

Li *et al. Satellite Navigation*   (2023) 4:26

Page 11 of 18
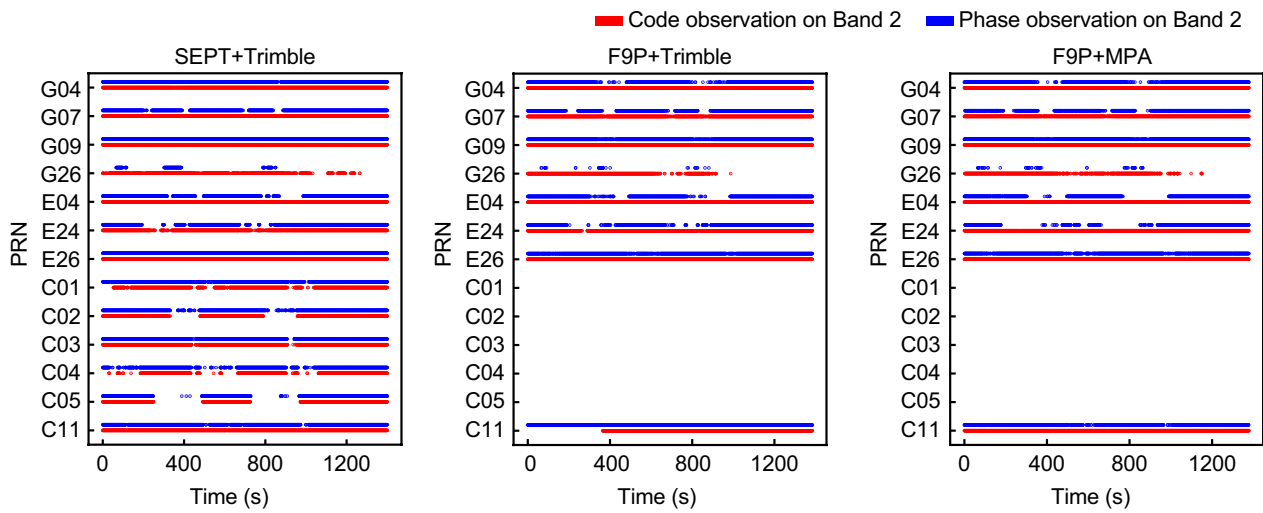
Fig. 7 Observation availability of the different GNSS devices

Table 4 Percentage of single-frequency data in different scenarios

Terminals	SEPT + Trimble (%)	F9P + Trimble (%)	F9P + VDA (%)	F9P + MPA (%)	F9P + HA (%)
Static	4.6	–	27.9	31.5	29.3
Low-speed	13.5	27.4	34.6	34.3	37.4
Vehicle	11.9	24.7	27.9	27.3	27.0
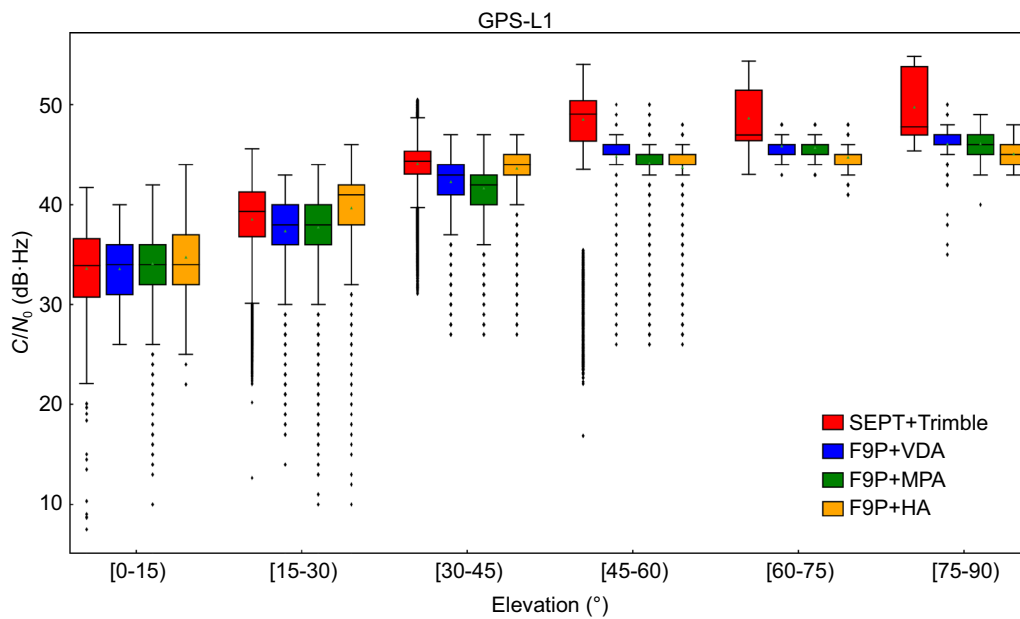
Fig. 8 C/N_0 of different GNSS terminals on L1 of GPS (red: SEPT + Trimble; blue: F9P + VDA; green: F9P + MPA; yellow: F9P + HA)

Li *et al. Satellite Navigation*　　　(2023) 4:26

Page 12 of 18
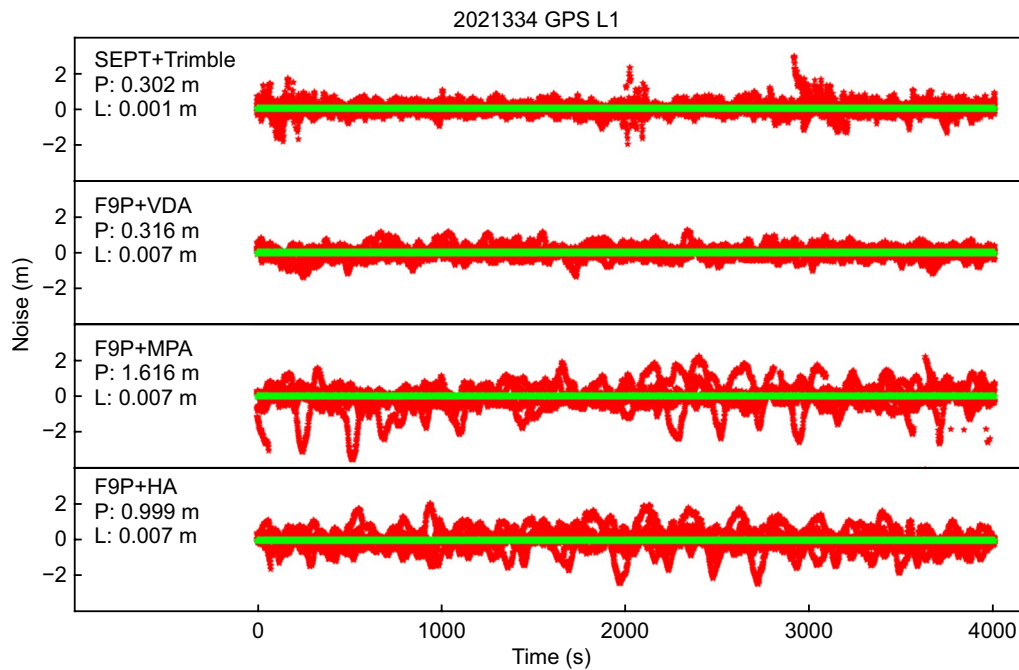
Fig. 9 Noise of different GNSS terminals on L1 of GPS in the static experiment. Red and green dots represent code and phase noise, respectively. The letters "P" and "L" depict the Root Mean Square (RMS) of code and phase noise, respectively

the low-cost F9P + MPA antenna has several outliers in the first red box, while the other two antennas demonstrate stable positioning performance. To investigate

the reason for this difference in performance, the cycle slips in the two periods are counted and shown in Table 8. It can be observed that the low-cost devices
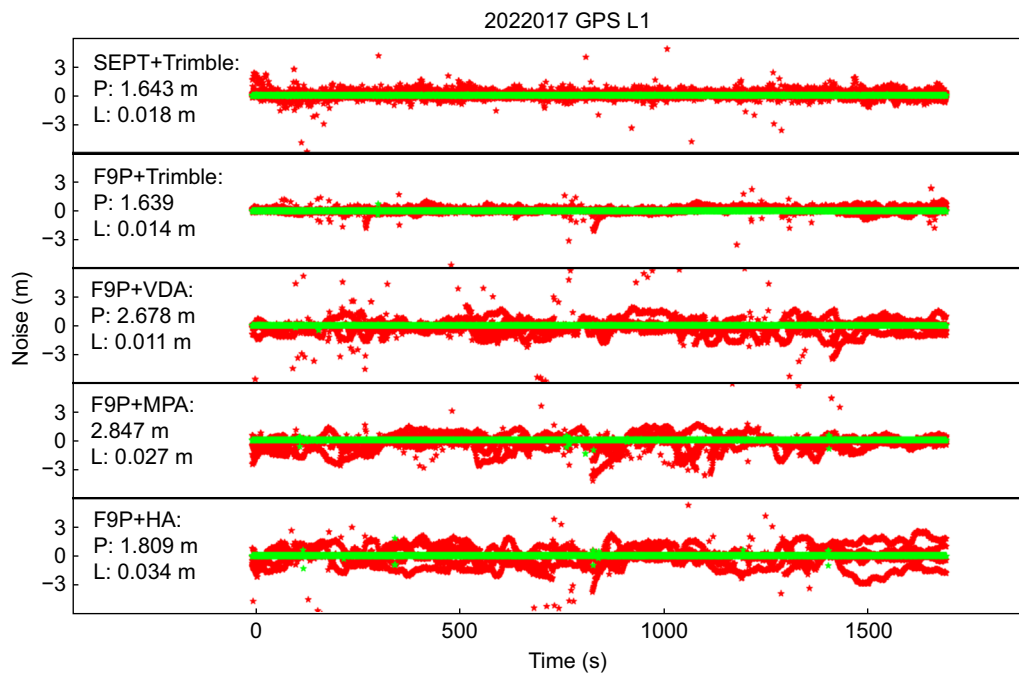
Fig. 10 Noise of different GNSS terminals on L1 of GPS on DOY 017, 2022. Red and green dots represent code and phase noise, respectively. The letters "P" and "L" depict the RMS of code and phase noise, respectively

Table 5 Cycle slip rate of different GNSS terminals

Terminals	Static results during 10 h		Kinematic results during 25 min	
	Cycle slip number	Cycle slip rate (‰)	Cycle slip number	Cycle slip rate (‰)
SEPT + Trimble	339	0.31	305	6.95
F9P + Trimble	–	–	888	24.75
F9P + VDA	1547	1.73	1054	30.17
F9P + MPA	2713	2.96	923	26.52
F9P + HA	1571	1.69	834	24.42

Table 6 Data quality ranking of different low-cost GNSS antennas

	C/N_0	Noise level (static)	Noise level (kinematic)	Cycle slip rate (static)	Cycle slip rate (kinematic)
Great	HA	VDA	MPA	HA	HA
↑	VDA	HA	VDA	VDA	MPA
Poor	MPA	MPA	HA	MPA	VDA

experience much more cycle slips than the geodetic one, and the F9P receiver with an MPA antenna is the most susceptible to cycle slips. This suggests that frequent cycle slips are the primary factor that affects the positioning performance of low-cost devices.

Table 9 shows the fixed rate and the positioning accuracy in the east, north, and up components. Among the four types of GNSS terminals, SEPT + Trimble and F9P + VDA perform best with a horizontal accuracy of 0.04 m and vertical accuracy of 0.07 m. F9P + HA with the positioning accuracy of (0.05 m, 0.03 m, 0.14 m) is slightly inferior to them, while F9P + MPA with the

positioning accuracy of (0.16 m, 0.14 m, 0.50 m) exhibits the worst performance in the fixed rate. This may be attributed to the frequent cycle slip and large noise level of F9P + MPA.

PPP-RTK performance in kinematic experiments

Figure 13 illustrates the positioning error series and data availability for selected satellites in a kinematic scenario with a low-cost u-blox receiver and a low-cost helix antenna. The graph clearly demonstrates the effectiveness of our PPP-RTK method, as it consistently achieves rapid centimeter-level positioning accuracy for most of the 15-min period. In contrast, the traditional dual-frequency PPP-RTK method can only use the satellites with dual-frequency data, leading to several reductions in the
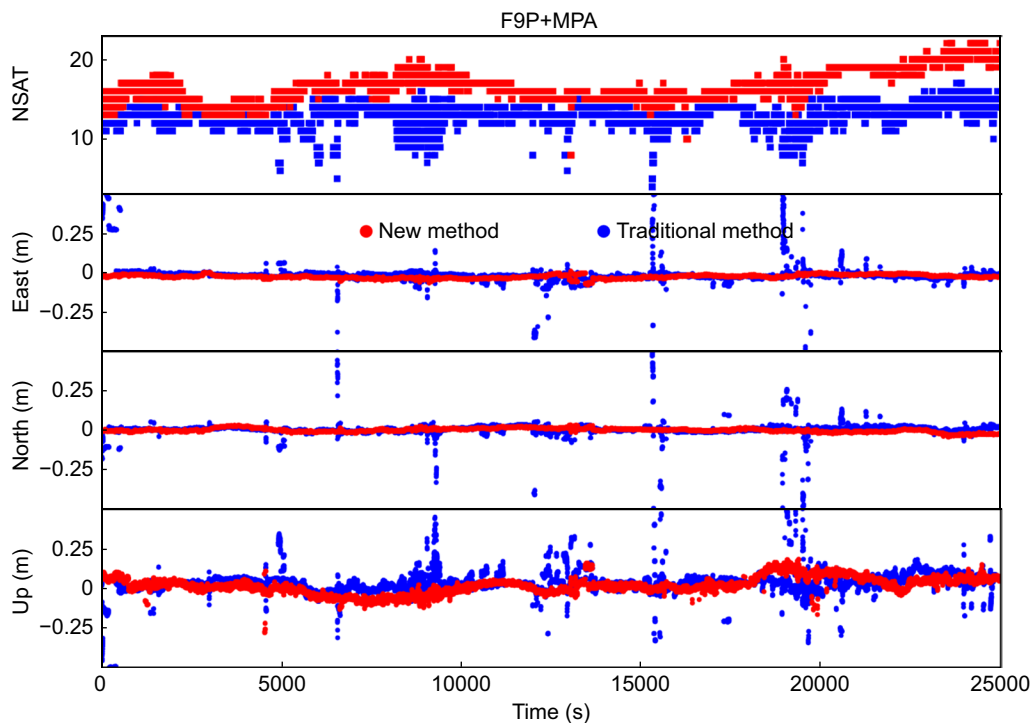
Fig. 11 Positioning error series and satellite numbers using a low-cost u-blox receiver with a microstrip patch antenna. The red and blue points represent the proposed method and the traditional one, respectively

Li *et al. Satellite Navigation* (2023) 4:26

Page 14 of 18

Table 7 Fixed rate and positioning accuracy of the new method and the traditional one

Method	Fixed rate (%)	RMS in different (east, north, up) directions (m)
Traditional method	97.6	(0.16, 0.10, 0.49)
New method	99.2	(0.03, 0.01, 0.06)

Table 8 Cycle slip rate of different GNSS terminals

Terminals	Results of Box1 area		Results of Box2 area	
	Cycle slip number	Cycle slip rate (‰)	Cycle slip number	Cycle slip rate(‰)
SEPT+Trimble	39	0.31	6	0.17
F9P+VDA	130	1.36	62	2.16
F9P+MPA	157	1.53	118	3.85
F9P+HA	101	0.99	71	2.36

number of available satellites and reconvergence processes, as depicted in the right panel of Fig. 13. Table 10 further presents the fixed rate and positioning accuracy. The 3D-RMS of our new method is reduced from 2.94 m of the traditional method to 0.46 m, an improvement by 84.3%.

Figure 14 depicts the positioning error series of all five GNSS terminals in kinematic Experiment A, and Table 11 reports their fixed rates and position accuracy. The SEPT + Trimble and F9P + Trimble perform best among all the terminals with a fixed rate of more than 99%. It illustrates that with the geodetic Trimble antenna the low-cost u-blox GNSS board can achieve the same positioning performance as the geodetic GNSS board Septentrio. Among the three low-cost GNSS devices, F9P+HA is the top performer with a positioning accuracy of (0.07 m, 0.07 m, 0.34 m), owing to its lower cycle slip rate and higher gain for low-elevation satellites. In contrast, F9P + VDA, which
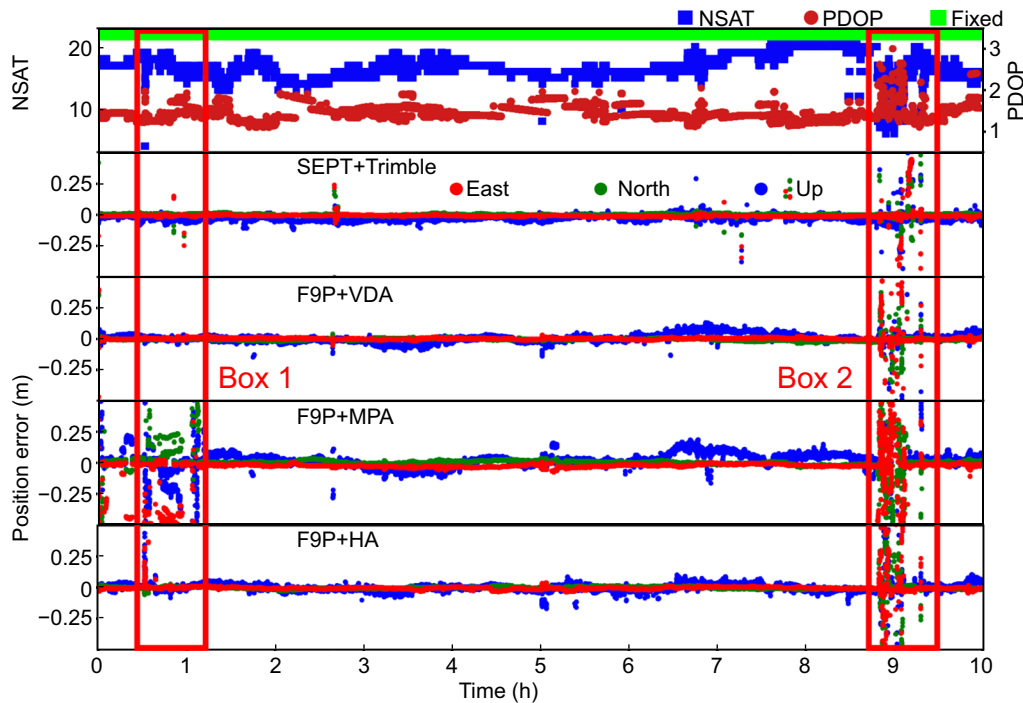
Table 9 Fixed rate and positioning accuracy of different GNSS terminals in static Experiment

Terminals	Fixed rate (%)	RMS in different (east, north, up) directions (m)
SEPT+Trimble	99.59	(0.03, 0.02, 0.07)
F9P+VDA	99.78	(0.02, 0.01, 0.07)
F9P+MPA	96.39	(0.16, 0.14, 0.50)
F9P+HA	99.62	(0.05, 0.03, 0.14)

performs best under static conditions, exhibits the worst performance in kinematic scenarios. We find that F9P + VDA exhibits a high cycle slip rate of 35.8‰ in the initial period, which impacts its positioning performance. Our results suggest that the combination of the

Fig. 12 Positioning errors of different GNSS terminals in the static experiment
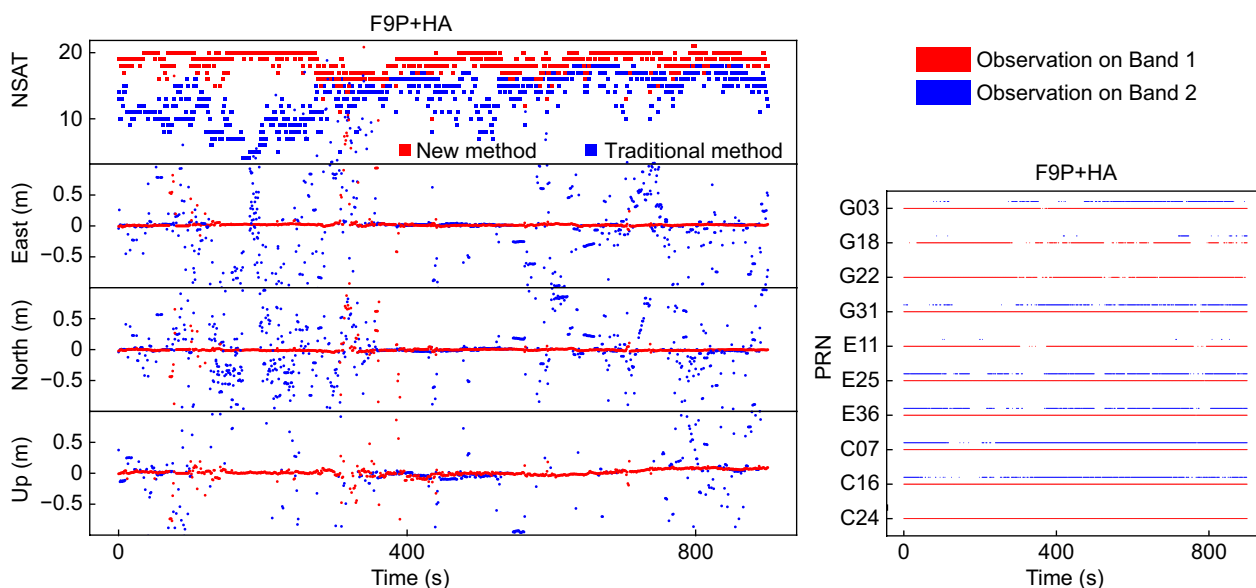
Fig. 13 Positioning errors series and data availability for selected satellites using a low-cost u-blox receiver with a helix antenna. In the positioning errors series on the left panel, the red and blue points represent the proposed method and the traditional one used, respectively. In the data availability on the right panel, the red and blue points represent the data on the first band and the second band, respectively

Table 10 Fixed rate and positioning accuracy of the new method and the traditional one

Method	Fixed rate (%)	RMS in different (east, north, up) directions (m)
Traditional method	80.6	(0.97, 0.77, 2.67)
New method	98.4	(0.23, 0.13, 0.38)

F9P receiver and helix antenna, which can achieve geodetic-level positioning performance, is the most suitable for kinematic applications.

Furthermore, Fig. 15 presents the position error series and satellite numbers of different devices in Experiment B. The number of available satellites (NSAT) of F9P + HA is also presented in the figure. It is worth noting that the number of available satellites for other devices is comparable to that of F9P + HA. During the first 18 min, the number of available GNSS satellites varies between 10 and 20, which ensures a continuous and reliable positioning. The F9P + HA configuration can achieve comparable positioning accuracy to that of SEPT + Trimble and F9P + Trimble. However, the positioning results obtained with F9P + MPA and F9P + VDA configurations are comparatively inferior. Then, the vehicle runs into a semi-urban environment with several trees, tall buildings, and overpasses where the signal tracking becomes discontinuous and the NSAT drops frequently. Because

of the frequent signal interruptions, the positioning accuracy of different devices, especially low-cost equipment, decreases. Notably, SEPT + Trimble and F9P + Trimble consistently achieve decimeter-level positioning accuracy, even in unfavorable observation conditions. However, the three low-cost devices exhibit poor performance. This phenomenon highlights the susceptibility of low-cost antennas to environmental interference.

Table 12 summarizes the fixed rate and positioning accuracy achieved by the different GNSS terminals during the first 18 min in a GNSS favorable scenario. SEPT + Trimble and F9P + Trimble exhibit the best performance, achieving centimeter-level accuracy with a fixed rate exceeding 99%. F9P + HA, which has the best performance in Experiment A, also outperforms the others in Experiment B with a horizontal accuracy of 0.2 m and vertical accuracy of 0.4 m. In contrast, F9P + VDA and F9P + MPA demonstrate poor positioning accuracy, despite their fixed rates of above 90%, due to the high incidence of wrongly fixed solutions. Hence, the helix antenna is the best choice among the three types of antennas under favorable kinematic scenarios.

Conclusions

This contribution proposed a modified PPP-RTK algorithm for the low-cost GNSS devices and evaluated its performance in different scenarios using different low-cost GNSS devices equipped with vertical dipole,
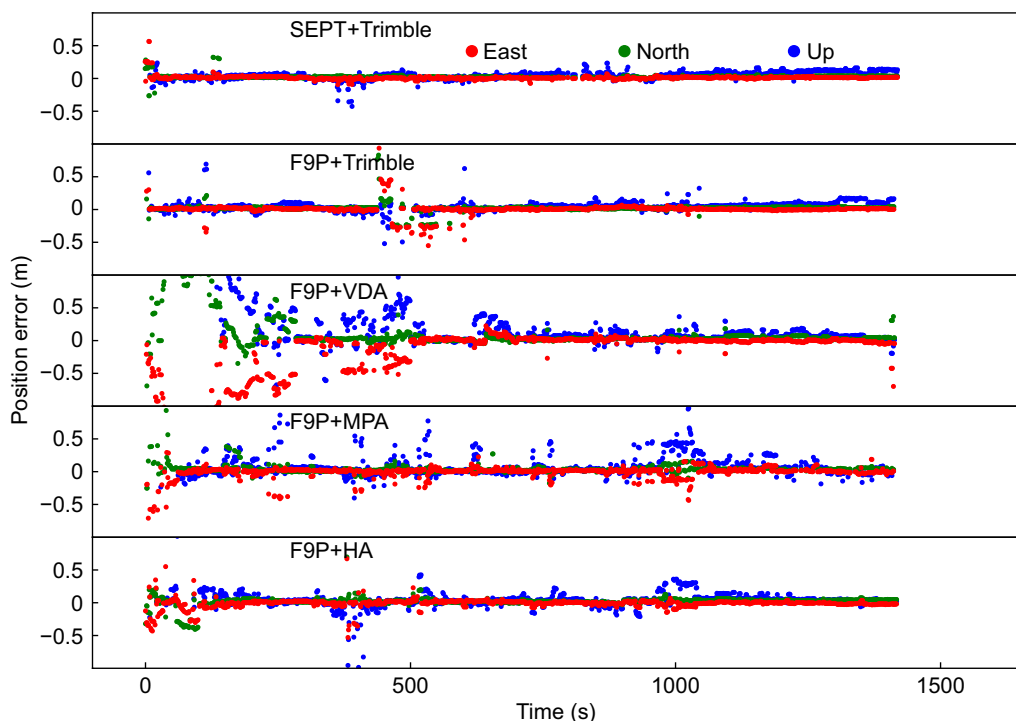
Fig. 14 Positioning errors of different GNSS terminals in experiment A

Table 11 Fixed rate and positioning accuracy of different GNSS terminals in Experiment A
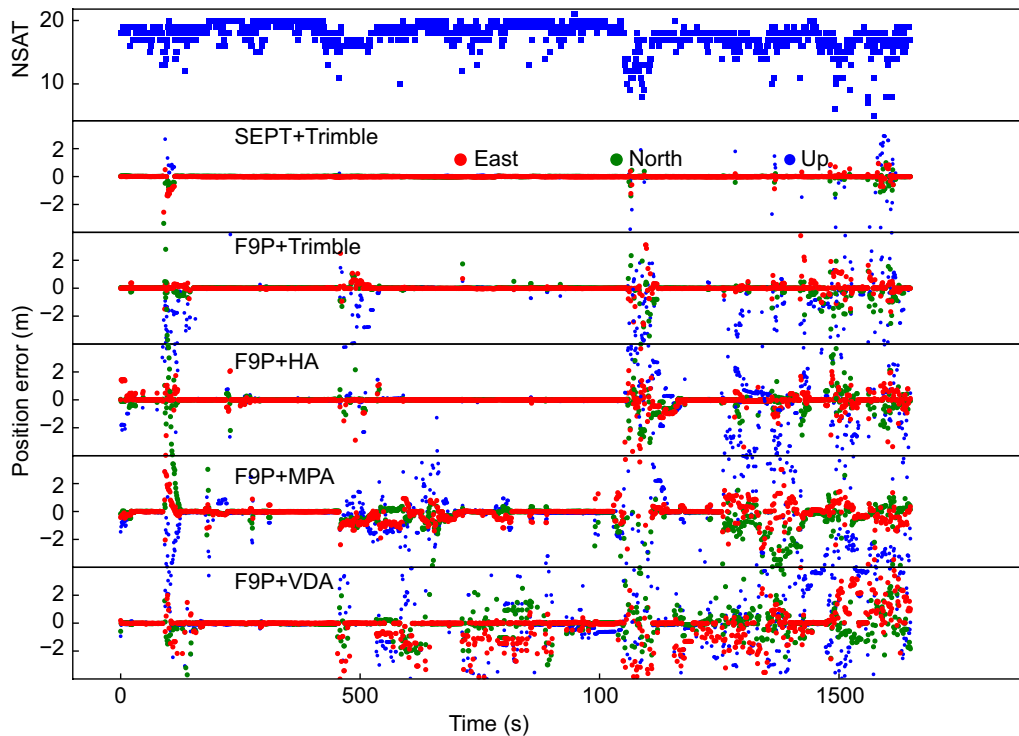
Terminals	Fixed rate (%)	RMS in different (east, north, up) directions (m)
SEPT + Trimble	99.3	(0.11, 0.07, 0.41)
F9P + Trimble	99.6	(0.12, 0.07, 0.37)
F9P + VDA	90.3	(0.41, 0.30, 1.65)
F9P + MPA	93.4	(0.09, 0.07, 0.34)
F9P + HA	95.3	(0.07, 0.07, 0.34)

microstrip patch, and helix antennas, respectively. The observation quality of different low-cost devices in terms of data availability, C/N_0, noise level, and cycle slip as well as the PPP-RTK positioning performance were investigated.

The experiment results illustrate that the ability to track satellites is determined by the GNSS board, while the continuity and integrity of the observations highly depend on the antenna. The helix antenna exhibits superior performance in C/N_0 compared to the other two low-cost antennas, approaching the level of a survey-grade Trimble antenna when the satellite elevation is below 45°. The microstrip patch antenna has the highest cycle slip rate under static conditions, while the vertical dipole antenna has the highest cycle slip rate under kinematic conditions. Furthermore, the level of measurement noise is also significantly affected by the type of GNSS antenna. In static mode, the code and phase noises of the three low-cost antennas range from 0.3–1.6 to 0.007 m, respectively, whereas in low-speed kinematic scenarios, they range from 1.8–2.8 to 0.011–0.034 m, respectively. In vehicle experiments, the noise level increases to 3.9 m and 0.3 m for code and phase noise, respectively.

Compared to the traditional PPP-RTK model, the proposed method shows a better performance with the positioning error decreasing from 0.53 to 0.07 m. Both the static and low-speed kinematic experiments demonstrate that centimeter-level positioning accuracy can be achieved with low-cost devices. The experiment results indicate that the vertical dipole antenna with the positioning accuracy of (0.02 m, 0.01 m, 0.07 m) performs best under static conditions, and the helix antenna exhibits the best performance with the positioning accuracy of (0.07 m, 0.07 m, 0.34 m) under the low-speed kinematic scenario among the three types of low-cost antennas. Additionally, the helix antenna is the best choice for vehicle navigation with a fixed rate of over 95%, a horizontal accuracy of 0.2 m, and a vertical accuracy of 0.4 m under favorable observation conditions.

Fig. 15 Positioning errors of different GNSS terminals in experiment A

Table 12 Fixed rate and positioning accuracy of different GNSS terminals in favorable scenario of Experiment B

Terminals	Fixed rate (%)	RMS in different (east, north, up) directions (m)
SEPT + Trimble	100.0	(0.02, 0.02, 0.06)
F9P + Trimble	99.1	(0.02, 0.06, 0.12)
F9P + HA	98.0	(0.13, 0.15, 0.36)
F9P + VDA	93.6	(0.77, 0.55, 1.79)
F9P + MPA	93.8	(0.47, 0.54, 0.95)

Author contributions
XXL, HG and XL provided the initial idea and wrote the manuscript; HL, YZ and H.W. helped perform the experiments; ZS and QZ helped analyze the data; All authors helped in writing, providing helpful suggestions, and reviewing the manuscript.

Availability of data and materials
The datasets of low-cost devices' GNSS observations are available on reasonable request from the corresponding author.

Declarations

Competing interests
The authors declare that they have no competing interests.

References
Amami, M. (2022). Testing patch, helix and vertical dipole GPS antennas with/ without choke ring frame. *International Journal for Research in Applied Sciences and Engineering Technology, 10*, 933–938.
Amami, M. M., Smith, M. J., & Kokkas, N. (2014). Low cost vision based personal mobile mapping system. *ISPRS-International Archives of the Photogrammetry, Remote Sensing and Spatial Information Sciences, 40*, 1–6.
Amiri-Simkooei, A., & Tiberius, C. (2007). Assessing receiver noise using GPS short baseline time series. *GPS Solutions, 11*, 21–35.
Bancroft, R. (2019). *Microstrip and printed antenna design.* Institution of Engineering and Technology.

Li *et al. Satellite Navigation*   (2023) 4:26

Page 18 of 18

Caldera, S., Realini, E., Barzaghi, R., Reguzzoni, M., & Sansò, F. (2016). Experimental study on low-cost satellite-based geodetic monitoring over short baselines. *Journal of Surveying Engineering, 142*, 04015016.

Chen, W., & Qin, H. (2012). New method for single epoch, single frequency land vehicle attitude determination using low-end GPS receiver. *GPS Solutions, 16*, 329–338.

Cina, A., & Piras, M. (2015). Performance of low-cost GNSS receiver for landslides monitoring: Test and results. *Geomatics, Natural Hazards and Risk, 6*, 497–514.

Garrido-Carretero, M. S., Borque-Arancón, M. J., Ruiz-Armenteros, A. M., Moreno-Guerrero, R., & Gil-Cruz, A. J. (2019). Low-cost GNSS receiver in RTK positioning under the standard ISO-17123-8: A feasible option in geomatics. *Measurement, 137*, 168–178.

Geng, J., Guo, J., Meng, X., & Gao, K. (2020). Speeding up PPP ambiguity resolution using triple-frequency GPS/BeiDou/Galileo/QZSS data. *Journal of Geodesy, 94*, 1–15.

Gill, M., Bisnath, S., Aggrey, J., & Seepersad, G. (2017). Precise point positioning (PPP) using low-cost and ultra-low-cost GNSS receivers. In *Proceedings of the 30th international technical meeting of the satellite division of the institute of navigation (ION GNSS+ 2017)* (pp. 226–2360).

Gogoi, N., Minetto, A., Linty, N., & Dovis, F. (2018). A controlled-environment quality assessment of android GNSS raw measurements. *Electronics, 8*, 5.

Håkansson, M., Jensen, A. B., Horemuz, M., & Hedling, G. (2017). Review of code and phase biases in multi-GNSS positioning. *GPS Solutions, 21*, 849–860.

Hamza, V., Stopar, B., & Sterle, O. (2021). Testing the performance of multi-frequency low-cost GNSS receivers and antennas. *Sensors, 21*, 2029.

Hofmann-Wellenhof, B., Lichtenegger, H., & Collins, J. (2012). *Global positioning system: Theory and practice*. Springer.

Huang, T. (2022). *Design and electromagnetic characterization of circularly-polarized shorted-annular-ring GPS antenna for autonomous rail vehicles positioning*. UCLA.

Jo, H., Sim, S. H., Tatkowski, A., Spencer, B., Jr., Nelson, M. E., & Monitoring, H. (2013). Feasibility of displacement monitoring using low-cost GPS receivers. *Structural Control, 20*, 1240–1254.

Kaplan, E. D., & Hegarty, C. (2017). *Understanding GPS/GNSS: Principles and applications*. Artech House.

Kleusberg, A., & Teunissen, P. J. (1996). *GPS for geodesy*. Springer.

Kouba J. (2009). *A guide to using international GNSS service (IGS) products*.

Li, B., Zang, N., Ge, H., & Shen, Y. (2019). Single-frequency PPP models: Analytical and numerical comparison. *Journal of Geodesy, 93*, 2499–2514.

Li, G., & Geng, J. (2019). Characteristics of raw multi-GNSS measurement error from Google Android smart devices. *GPS Solutions, 23*, 1–16.

Li, G., & Geng, J. (2022). Android multi-GNSS ambiguity resolution in the case of receiver channel-dependent phase biases. *Journal of Geodesy, 96*, 72.

Li, X., Han, X., Li, X., Liu, G., Feng, G., Wang, B., & Zheng, H. (2021). GREAT-UPD: An open-source software for uncalibrated phase delay estimation based on multi-GNSS and multi-frequency observations. *GPS Solutions, 25*, 1–9.

Li, X., Wang, H., Li, X., Li, L., Lv, H., Shen, Z., Xia, C., & Gou, J. (2022). PPP rapid ambiguity resolution using Android GNSS raw measurements with a low-cost helical antenna. *Journal of Geodesy, 96*, 65.

Li, X., Zhang, X., & Ge, M. (2011). Regional reference network augmented precise point positioning for instantaneous ambiguity resolution. *Journal of Geodesy, 85*, 151–158.

Mi, X., Zhang, B., & Yuan, Y. (2019). Multi-GNSS inter-system biases: Estimability analysis and impact on RTK positioning. *GPS Solutions, 23*, 1–13.

Mongrédien, C., Doyen, J.-P., Strom, M., & Ammann, D. (2016). Centimeter-level positioning for UAVs and other mass-market applications. In *Proceedings of the 29th international technical meeting of the satellite division of the institute of navigation (ION GNSS+ 2016)* (pp. 1441–1454).

Nadarajah, N., Khodabandeh, A., Wang, K., Choudhury, M., & Teunissen, P. J. (2018). Multi-GNSS PPP-RTK: From large- to small-scale networks. *Sensors, 18*, 1078.

Nie, Z., Liu, F., & Gao, Y. (2020). Real-time precise point positioning with a low-cost dual-frequency GNSS device. *GPS Solutions, 24*, 1–11.

NovAtel. (2018). *Inertial Explorer 8.70 user manual*. https://novatel.com/support/support-materials/manual

Odolinski, R., & Teunissen, P. J. (2016). Single-frequency, dual-GNSS versus dual-frequency, single-GNSS: A low-cost and high-grade receivers GPS-BDS RTK analysis. *Journal of Geodesy, 90*, 1255–1278.

Odolinski, R., & Teunissen, P. J. (2017). Low-cost, high-precision, single-frequency GPS–BDS RTK positioning. *GPS Solutions, 21*, 1315–1330.

Pirazzi, G., Mazzoni, A., Biagi, L., & Crespi, M. (2017). Preliminary performance analysis with a GPS+ Galileo enabled chipset embedded in a smartphone. In *Proceedings of the 30th international technical meeting of the satellite division of the institute of navigation (ION GNSS+ 2017)* (pp. 101–115).

Psychas, D., & Verhagen, S. (2020). Real-time PPP-RTK performance analysis using ionospheric corrections from multi-scale network configurations. *Sensors, 20*, 3012.

Takasu, T., & Yasuda, A. (2008). Evaluation of RTK-GPS performance with low-cost single-frequency GPS receivers. In *Proceedings of international symposium on GPS/GNSS* (pp. 852–861).

Takasu, T., & Yasuda, A. (2009). Development of the low-cost RTK-GPS receiver with an open source program package RTKLIB. In *International symposium on GPS/GNSS* (pp. 1–6). Jeju: International Convention Center.

Temiissen, J. (1995). The least-squares ambiguity decorrelation adjustment: A method for fast GPS integer ambiguity estimation. *Journal of Geodesy, 70*, 65–82.

Teunissen, P. J. (2018). Distributional theory for the DIA method. *Journal of Geodesy, 92*, 59–80.

Teunissen, P. J. G., Odijk, D., & Zhang, B. (2010). PPP-RTK: Results of CORS network-based PPP with integer ambiguity resolution. *J Aeronaut Astronaut Aviat Ser A, 42*, 223–230.

Wang, J., Satirapod, C., & Rizos, C. (2002). Stochastic assessment of GPS carrier phase measurements for precise static relative positioning. *Journal of Geodesy, 76*, 95–104.

Wang, L., Li, Z., Wang, N., & Wang, Z. (2021). Real-time GNSS precise point positioning for low-cost smart devices. *GPS Solutions, 25*, 1–13.

Wanninger, L., & Heßelbarth, A. (2020). GNSS code and carrier phase observations of a Huawei P30 smartphone: Quality assessment and centimeter-accurate positioning. *GPS Solutions, 24*, 1–9.

Wen, Q., Geng, J., Li, G., & Guo, J. (2020). Precise point positioning with ambiguity resolution using an external survey-grade antenna enhanced dual-frequency android GNSS data. *Measurement, 157*, 107634.

Wübbena, G., Schmitz, M., & Bagge, A. (2005). PPP-RTK: precise point positioning using state-space representation in RTK networks. In *Proceedings of the 18th international technical meeting of the satellite division of the institute of navigation (ION GNSS 2005)* (pp. 2584–2594).

Zhang, B., Chen, Y., & Yuan, Y. (2019a). PPP-RTK based on undifferenced and uncombined observations: Theoretical and practical aspects. *Journal of Geodesy, 93*, 1011–1024.

Zhang, Z., Li, B., Gao, Y., & Shen, Y. (2019b). Real-time carrier phase multipath detection based on dual-frequency C/N0 data. *GPS Solutions, 23*, 1–13.

Zhang, Z., Yuan, H., Li, B., He, X., & Gao, S. (2021). Feasibility of easy-to-implement methods to analyze systematic errors of multipath, differential code bias, and inter-system bias for low-cost receivers. *GPS Solutions, 25*, 1–14.

Publisher's Note